

Mapping Local Climate Zones in Lausanne (Switzerland) with Sentinel-2 and PRISMA imagery: comparison of classification performance using different band combinations and building height data

Alberto Vavassori, Gregory Giuliani & Maria Antonia Brovelli

To cite this article: Alberto Vavassori, Gregory Giuliani & Maria Antonia Brovelli (2023) Mapping Local Climate Zones in Lausanne (Switzerland) with Sentinel-2 and PRISMA imagery: comparison of classification performance using different band combinations and building height data, International Journal of Digital Earth, 16:2, 4790-4810, DOI: [10.1080/17538947.2023.2283485](https://doi.org/10.1080/17538947.2023.2283485)

To link to this article: <https://doi.org/10.1080/17538947.2023.2283485>



© 2023 The Author(s). Published by Informa UK Limited, trading as Taylor & Francis Group



[View supplementary material](#)



Published online: 15 Nov 2023.



[Submit your article to this journal](#)



Article views: 435






[View related articles](#)



[View Crossmark data](#)

Mapping Local Climate Zones in Lausanne (Switzerland) with Sentinel-2 and PRISMA imagery: comparison of classification performance using different band combinations and building height data

Alberto Vavassori ^a, Gregory Giuliani ^b and Maria Antonia Brovelli ^a

^aDepartment of Civil and Environmental Engineering, Politecnico di Milano, Milano, Italy; ^bInstitute for Environmental Sciences, University of Geneva, Geneva, Switzerland

ABSTRACT

The Local Climate Zone (LCZ) concept has emerged as a valuable classification system for climate-related studies. The World Urban Database and Access Portal Tools (WUDAPT) protocol provides a framework for generating a LCZ segmentation which relies on the supervised classification of multispectral imagery. However, since LCZ is based on the physical and thermal properties of the urban surfaces, more insightful information on the surface reflectivity characteristics – which is provided by hyperspectral sensors – may be beneficial for improving the LCZ classification. This assumption is investigated in this study by comparing the classification performance of a supervised algorithm applied to multispectral (Sentinel-2) and hyperspectral (PRISMA) satellite imagery. The study area is the city of Lausanne (Switzerland). Experiments are performed considering these sensors and different band combinations, including the building height layer as an additional band. Preliminary outcomes show that PRISMA imagery yields satisfying results in terms of classification accuracy while not outperforming Sentinel-2. An improvement is achieved by leveraging the first 10 PRISMA Principal Components which allows to retain the uncorrelated information out of the original bands. These first results will be validated in future investigations by improving image pre-processing and exploiting a larger number of seasonal PRISMA acquisitions.

ARTICLE HISTORY

Received 31 January 2023
Accepted 9 November 2023


KEYWORDS

Local Climate Zones;
Sentinel-2; PRISMA;
supervised classification;
building height

1. Introduction

The Sustainable Development Goal 11 of the United Nations stresses the importance of making cities and human settlements ‘inclusive, safe, resilient and sustainable’ (<https://www.un.org/sustainabledevelopment>). With the concentration of people, infrastructures, and strategic assets, the urban environment is particularly sensitive to the negative effects of climate change. A well-known effect induced by climate change and increasing urbanisation consists in the intensification of the urban heat island (Chapman et al. 2019). This phenomenon has caught the attention of the scientific community which in the last few decades has developed physical models capable to

CONTACT Gregory Giuliani  Gregory.Giuliani@unige.ch  Institute for Environmental Sciences, University of Geneva, 66 Boulevard Carl-Vogt, CH - 1205 Geneve, Switzerland

 Supplemental data for this article can be accessed online at <https://doi.org/10.1080/17538947.2023.2283485>

This article has been corrected with minor changes. These changes do not impact the academic content of the article.

© 2023 The Author(s). Published by Informa UK Limited, trading as Taylor & Francis Group
This is an Open Access article distributed under the terms of the Creative Commons Attribution License (<http://creativecommons.org/licenses/by/4.0/>), which permits unrestricted use, distribution, and reproduction in any medium, provided the original work is properly cited. The terms on which this article has been published allow the posting of the Accepted Manuscript in a repository by the author(s) or with their consent.

measure its intensity and identify its driving factors (Kim and Brown 2021). With the rapid spread of advanced Earth Observation (EO) technologies, the study of the urban heat island effect has further deepened thanks to the availability of homogeneous, high-resolution, and global-coverage data. Among the numerous global initiatives, the Copernicus Programme is empowering a wide range of end-users – including public authorities and international organisations – with multiple geospatial data and information for environmental monitoring, emergency mapping, and climate change analysis (<https://www.copernicus.eu/en/copernicus-services>).

An effective tool to measure the urban heat island effect is represented by a climate-centred classification system called Local Climate Zone (LCZ) (Stewart and Oke 2012). The LCZ concept defines 17 classes based on the physical and thermal properties of the urban and natural surfaces. Specifically, the area types are divided into 10 ‘built-up’ and 7 ‘natural’ classes depending on the morphological characteristics (height and density of buildings and trees) and land cover composition (impervious and pervious surfaces) of the urban and natural environment. Such classification system has been exploited in several research studies connected with the investigation of local temperature patterns, micro-climate analyses, and anthropogenic heat fluxes quantification (Kotharkar et al. 2022; Stewart, Oke, and Krayenhoff 2013; Verdonck et al. 2018). Also, LCZ maps are leveraged as an input for several models which are used for local weather prediction as well as air quality and energy use applications (Betchel et al. 2019a; Ching et al. 2018).

Different methodologies have been developed to produce LCZ maps. A recent work of literature review (Aslam and Rana 2022) has provided insights into the data sources, procedures, and algorithms that are most frequently adopted for this purpose. Specifically, the protocol defined within the World Urban Database and Access Portal Tools (WUDAPT) (<http://www.wudapt.org>; Bechtel et al. 2015), which relies on the supervised classification of multispectral satellite imagery, is a benchmark for LCZ mapping. WUDAPT also provides access to LCZ maps of different cities. Alternative methodologies include Geographic Information System (GIS) based approaches that consist in the reclassification of existing vector and raster layers (Bocher et al. 2021); despite their advantages, data needed for their application is not always readily-available which often prevents these methods from being easily replicated. The novel GIS based method presented in (Oliveira, Lopes, and Niza 2020) attempts to overcome this limitation by directly translating Copernicus services’ datasets (namely, the Urban Atlas and the Corine Land Cover layers) into LCZ maps within a GIS environment. The WUDAPT approach offers the best precision despite requiring expertise with GIS software and satellite imagery processing. On the other hand, GIS based methods yield fast computational performance, however, the final map quality is strictly dependent on the reclassification of the existing datasets (Sigler, Gilabert, and Villalba 2022).

Based on the literature summarised above, the most frequently used datasets for LCZ mapping include multispectral satellite imagery – mainly Landsat (5, 7, and 8) and Sentinel (1 and 2) images (Sukhanov et al. 2017) – and existing geospatial datasets – primarily retrieved from the WUDAPT database, land cover maps (Mouzourides et al. 2019), and OpenStreetMap (Bechtel et al. 2019). Field surveys may also be exploited to refine training polygons and for ground-truthing (Mushore et al. 2019).

Nonetheless, since the LCZ subdivision is strictly related to the physical and thermal properties of the urban and natural surfaces, a detailed description of the surface reflectivity properties might be beneficial for improving the LCZ classification performance. Hyperspectral sensors may provide crucial information for this purpose, since they record spectral signals in hundreds of narrow bands, thus enabling the capture of more continuous spectral characteristics of a ground feature than multispectral images (Lu, He, and Dao 2019). However, the use of space-borne hyperspectral sensors for LCZ mapping has not yet been widely used (Liang et al. 2023). Consequently, the aim of this study, is to compare multispectral and hyperspectral satellite sensors from Sentinel-2 and PRISMA (Hyperspectral Precursor of the Application Mission) missions. Sentinel-2 and PRISMA images are provided by the European Copernicus Programme and the Italian Space Agency (ASI), respectively. The City of Lausanne (Canton of Vaud, Switzerland) is considered as a case study because of its diversity of landscape features (e.g. dense urban centre, highly vegetated areas). Several

acquisitions of the two satellite missions are processed with the aim of accounting for the seasonal variations in the land cover composition (vegetative and non-vegetative periods) as well as increasing classification accuracy, as found in (Fung, Yang, and Niyogi 2022a). The Random Forest (RF) supervised algorithm is applied to several band combinations of the two sensors for each acquisition date and classification performance in terms of map accuracy is assessed. To our knowledge, such comparison has never been made between Sentinel-2 and PRISMA and could help providing insights into the optimal sensor and band combination to be used for LCZ mapping.

The remainder of the work is structured as follows. Section 2 presents the study area and the data sources used for the analysis. In Section 3 the methodology undertaken to process the datasets, compute the LCZ maps, and assess the classification accuracy are presented. Section 4 discusses the results achieved. Finally, in Section 5 the main conclusions of this work are outlined.

2. Materials

2.1. Study area

The study area considered in this work is the city of Lausanne (Canton of Vaud, Western Switzerland) (see Figure 1). The city is located on the northern shore of Lake Geneva which significantly influences

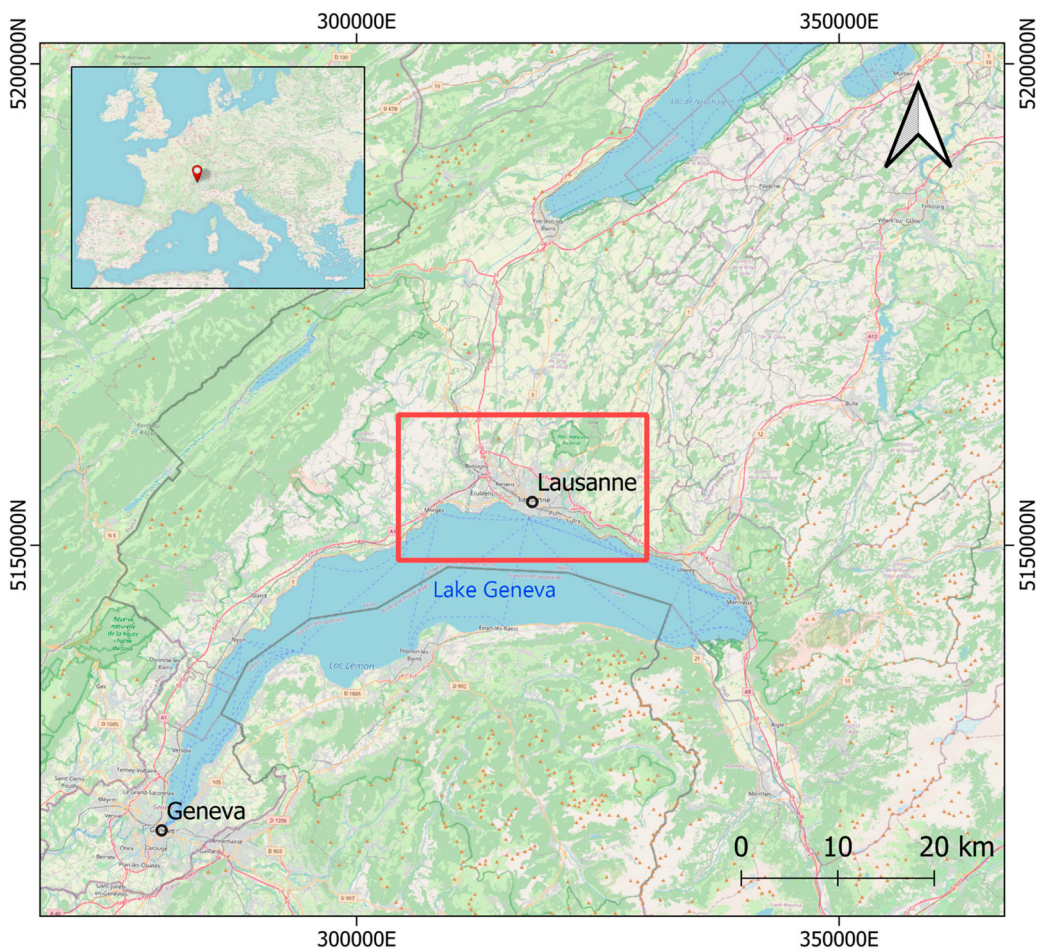


Figure 1. Location of the study area. Coordinate Reference System (CRS): WGS84/UTM zone 32 N. Map data: OpenStreetMap contributors.

the local climate by buffering extreme temperatures. According to the Köppen-Geiger Climate Classification, the city has a temperate climate, with no dry season and warm summer (Cfb zone) (Köppen 1884). Based on the official measurements of the Lausanne-Pully weather station, the maximum and minimum monthly temperature experienced in the area varies between 16.2°C and 25.0°C in July (warmest month), and 0.7°C and 4.7°C in January (coolest month) (<https://www.meteosuisse.admin.ch/services-et-publications/applications/ext/climate-climsheet.html>).

The urban setting of Lausanne is characterised by dense and high historical buildings in the central parts of the city, while modern and lower residential buildings are spread in the surrounding neighbourhoods. The city is surrounded by hills (with a maximum altitude of 900 m above sea level) covered with natural areas including rural zones and forested lands (Copernicus Urban Atlas 2018).

2.2. Satellite imagery: Sentinel-2 and PRISMA missions

Collected data consists mainly of optical satellite imagery and ancillary geospatial datasets. Specifically, multispectral Sentinel-2 and hyperspectral PRISMA images were exploited for LCZ mapping. Despite the different spatial resolution compared to PRISMA, Sentinel-2 was chosen among the available multispectral satellite missions – such as Landsat 8 – since it encompasses the same region of the electromagnetic spectrum as PRISMA, namely the Visible and Near InfraRed (VNIR) and Short-Wave InfraRed (SWIR) spectral bands. This guarantees a consistent comparison of the classification outputs. A detailed description of the two data sources is reported in the following.

Sentinel-2: The two Sentinel-2 satellites (launched on 23 June 2015 and 7 March 2017) acquire multispectral imagery in 13 spectral bands with a revisiting time of approximately 5 days. Bands from 2 to 8A and from 11 to 12 – originally provided with 10 or 20 m spatial resolution – were considered in this study. Sentinel-2 imagery is distributed under a fully open license through the Copernicus Access Hub interface (<https://scihub.copernicus.eu>), which provides different level products. In this study, the Level 2A product was used which consists in ortho-corrected data with pixel radiometric measurements provided in Bottom of Atmosphere (BoA) reflectance.

PRISMA: The PRISMA satellite (launched on 22 March 2019), owned and managed by ASI, acquires hyperspectral imagery in 240 spectral bands of the VNIR and SWIR regions of the electromagnetic spectrum. The hyperspectral camera acquires data with high spectral resolution (<14 nm) and medium spatial resolution (30 m). Also, a single-channel panchromatic (PAN) camera offers added capability with 5 m spatial resolution. Only the VNIR and SWIR data were exploited in this work. Access to PRISMA data is made available through the ASI dedicated portal (<https://prisma.asi.it>) with different level products. In this study, the Level 2D product was used which refers to the geocoded BoA reflectance data. Unlike Sentinel-2 imagery, PRISMA data is distributed under a ‘quasi-open’ data policy, meaning that: (i) user registration and licence explicit acceptance is required, (ii) products use is allowed only for scientific research purposes, and (iii) products cannot be redistributed.

Only satellite imagery with very limited cloud cover (i.e. < 5%) was chosen with the aim of generating LCZ maps. Date selection was strongly conditioned by the limited availability of PRISMA acquisitions on the area of study. Specifically, only four PRISMA acquisitions were available with low cloud cover. Sentinel-2 images were selected in such a way as to be as close as possible in time to the corresponding PRISMA acquisitions. Accordingly, four acquisitions of Sentinel-2 were considered overall. The dates and times of acquisition of the satellite images are reported in Table 1.

2.3. Ancillary datasets

Support datasets were leveraged for the visual identification of the LCZ classes in the study area as well as for the construction of independent training and testing samples. Specifically, ancillary

Table 1. Acquisition date and time for Sentinel-2 and PRISMA images. Time is given in Greenwich Mean Time (GMT).

Sentinel-2	PRISMA
12 August 2021 10:38 am	14 August 2021 10:40 am
6 September 2021 10:38 am	6 September 2021 10:37 am
28 February 2022 10:38 am	27 February 2022 10:40 am
25 March 2022 10:38 am	28 March 2022 10:40 am

datasets include: (i) very high-resolution Google satellite imagery, retrieved through the QuickMap-Service plugin in QGIS; (ii) the Copernicus Urban Atlas product (<https://land.copernicus.eu/local/urban-atlas>), updated to the year 2018; (iii) and the building height dataset of the Canton of Vaud. Only the former two layers are open geodata since it was not possible to retrieve a reliable open building height layer for the city of study. These datasets provided insightful pieces of information about the urban morphological characteristics and were thus exploited to identify uniform regions in terms of height and density of buildings, land cover, and land use. Accordingly, training and testing polygons were digitised in QGIS and selected according to the LCZ classification system.

3. Methods

3.1. Local climate zone (LCZ) mapping

In the city of Lausanne, 7 LCZ classes were found and considered out of the 17 original classes. **Table 2** reports a brief description of each class.

LCZ mapping was carried out by applying a supervised classification algorithm to the satellite imagery. For this reason, training and testing samples for each LCZ class were independently collected to train the classifier and assess the classification accuracy, respectively. Both training and testing samples were selected through a combined analysis of the available ancillary geodata. Polygons were selected in such a way to be uniformly distributed among the existing LCZ types, with the aim of guaranteeing an even representation of the different classes and increasing classification accuracy. The same training and testing datasets were exploited for the classification of all satellite images to properly compare the classification performance and provide a consistent accuracy assessment.

The spatial distribution of training and testing samples is depicted in **Figure 2**, while the total area of training and testing sets per LCZ types is reported in the Supplementary Material.


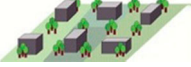
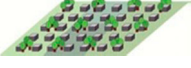

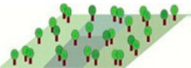


To perform the LCZ classification with Sentinel-2 and PRISMA imagery, several steps were required which are summarised in **Figure 3** and described in detail in the following sections.

3.2. Sentinel-2 imagery pre-processing

With the aim of performing LCZ classification, standard pre-processing steps were carried out. As for Sentinel-2 imagery, the Level 2A product used in this work does not need any atmospheric correction, since the band pixels are provided in real reflectance values. However, as Sentinel-2 images were exploited as a reference for PRISMA image pre-processing, some preliminary operations were carried out. Specifically, Sentinel-2 bands were resampled at 30 m spatial resolution (i.e. the same spatial resolution as PRISMA bands) through bilinear interpolation. The reason of this choice is twofold. On the one hand, it is a necessary step to apply the co-registration algorithm, as explained in the following Section. Also, for the purposes of comparing the classification performance using different spectral resolutions and band combinations, a different spatial resolution could partially bias the analysis.

Each acquisition was then re-projected to the cartographic reference system WGS84/UTM zone 32 N and clipped to the corresponding PRISMA image extent. Finally, image bands were merged in a single multiband raster in QGIS.

Table 2. Local Climate Zone (LCZ) classes retained for the city of Lausanne: Name and Description. Images are taken from (Stewart and Oke 2012).

Class name	Description
 <p>Compact mid-rise</p>	<p>Dense mix of midrise buildings (3-9 stories). Few or no trees. Land cover mostly paved. Stone, brick, tile, and concrete construction material.</p>
 <p>Open mid-rise</p>	<p>Open arrangement of mid-rise buildings (3-9 stories). Abundance of pervious land cover (low plants, scattered trees). Concrete, steel, stone, and glass construction materials.</p>
 <p>Open low-rise</p>	<p>Open arrangement of low-rise buildings (1-3 stories). Abundance of pervious land cover (low plants, scattered trees). Wood, brick, stone, tile, and concrete construction materials.</p>
 <p>Large low-rise</p>	<p>Open arrangement of large low-rise buildings (1–3 stories). Few or no trees. Land cover mostly paved. Steel, concrete, metal, and stone construction materials.</p>
 <p>Scattered trees</p>	<p>Lightly wooded landscape of deciduous and/or evergreen trees. Land cover mostly pervious (low plants). Zone function is natural forest, tree cultivation, or urban park.</p>
 <p>Low plants</p>	<p>Featureless landscape of glass or herbaceous plants/crops. Few or no trees. Zone function is natural grassland, agriculture, or urban park.</p>
 <p>Water</p>	<p>Large, open water bodies such as seas or lake, or small bodies such as rivers, reservoirs, and lagoons.</p>

3.3. PRISMA imagery pre-processing

PRISMA imagery required longer pre-processing steps that were mainly carried out through Python scripting. The Level 2D product used in this study refers to the geocoded BoA reflectance data, therefore no additional atmospheric correction was performed. The VNIR and SWIR data cubes were read according to the Hierarchical Data Format (HDF5) standard. Detailed information about PRISMA HDF5 format is available within the PRISMA products specification document (PRISMA Products Specification Document 2020). Bands affected by severe striping were removed which is due to a temporary unbalanced response of a VNIR or SWIR detector. This resulted in a total number of 234 bands (63 in VNIR and 171 in SWIR) that were assembled in a single image stack to be further manipulated.

As a second step, image geo-referencing was improved, since the geometric localisation errors of PRISMA imagery may be quite relevant (i.e. up to 200 m) when ground control points are not present over the acquisition area. The Sentinel-2 temporally closest acquisition was used as a reference to improve each PRISMA acquisition geo-referencing. Specifically, image co-registration was carried out through a custom Python code that was developed by the authors. The code takes

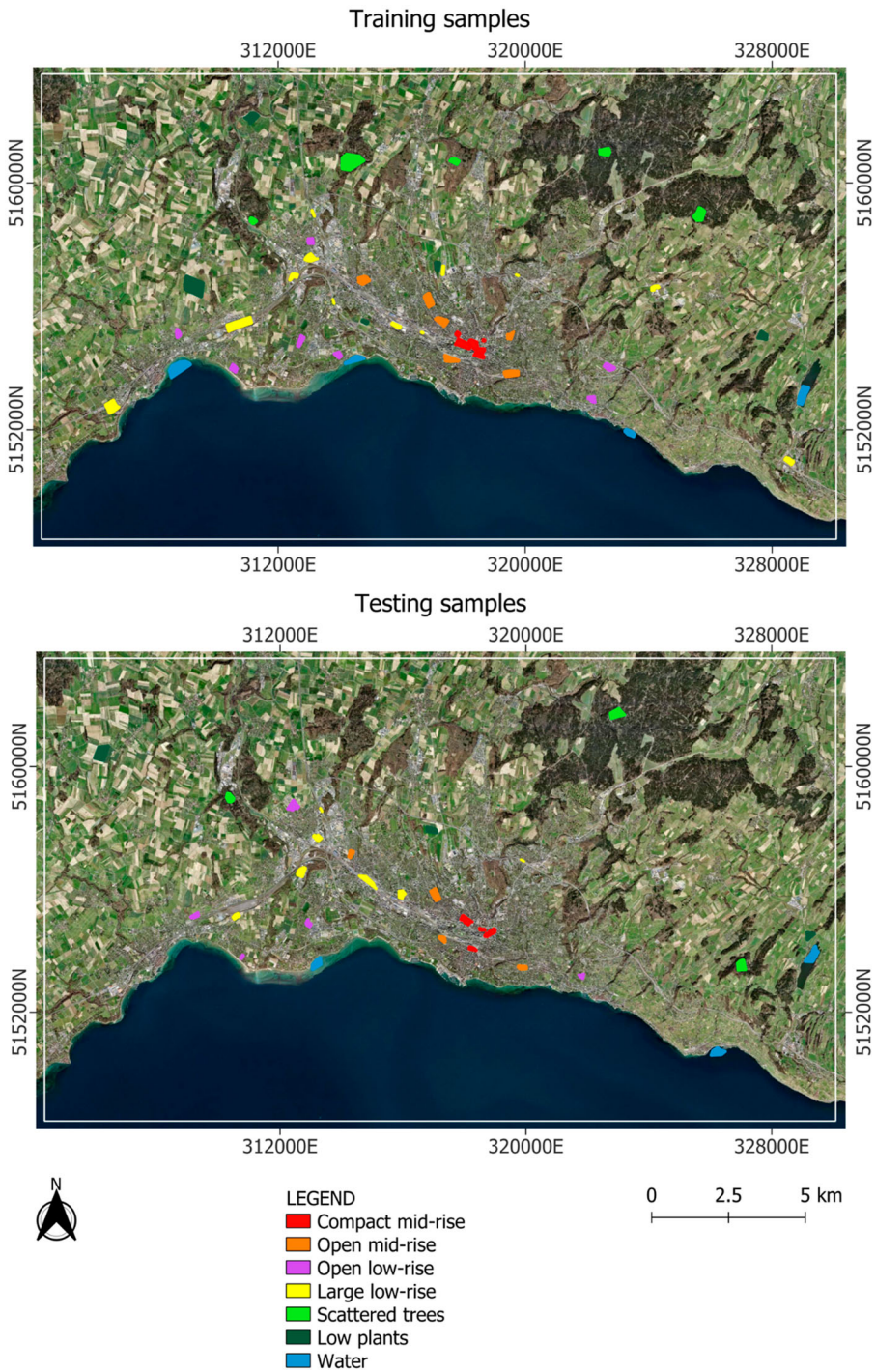


Figure 2. Distribution of training (above) and testing (below) samples exploited for LCZ classification. Map data: ESRI Satellite.

advantage of the GeFolki (i.e. Geoscience Extended Flow Optical Lucas-Kanade Iterative algorithm) Python package which is a dense and nonparametric method based on optical-flow computation for image co-registration (<https://github.com/aplyer/gefolki>; Brigot et al. 2016). In this work, the

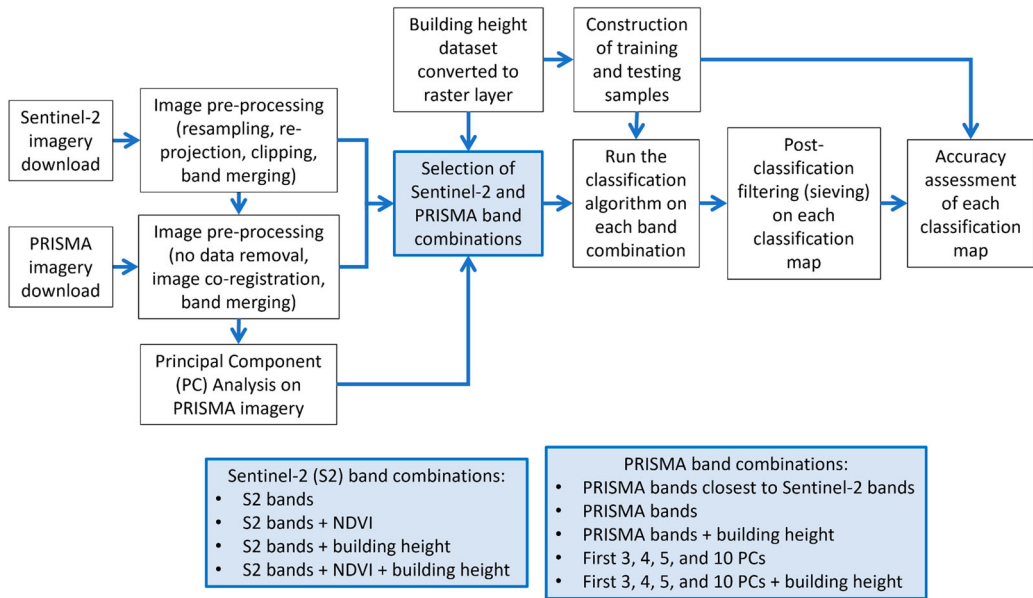


Figure 3. Flowchart adopted for the classification of date-specific Sentinel-2 and PRISMA imagery using different band combinations.

displacement field was estimated on the 571 nm band of PRISMA, considering the green band (560 nm) of Sentinel-2 (resampled at 30 m spatial resolution) as a reference. The estimated displacement field was then applied to all VNIR and SWIR bands of PRISMA which are already co-registered in the original product provided by ASI. The co-registered PRISMA bands were finally exported as GeoTIFF files and merged into a single multiband raster.

An example of the displacement field estimated with GeFolki is represented in [Figure 4](#), which refers to the PRISMA acquisition date 6 September 2021. In [Figure 4](#) the displacement field was resampled from 30 m to 1 km spatial resolution to allow for a best readability of the map. For the same reason, the arrow length is proportional to the actual displacement value albeit not drawn to scale. Outside the black frame, the displacement field is applied to no-data values which are then discarded in the analysis.

3.4. Selection of the band combinations

With the aim of finding the most suitable sensor and band set for mapping the LCZ distribution across the study area, several band combinations were assembled and tested. Beside the information provided by the spectral bands of the two satellite sensors, the building height layer was also exploited as an additional feature to improve the classification accuracy of the built-up LCZ types. Accordingly, the building height vector dataset was converted to a raster layer at 30 m resolution. The band combinations considered for the Sentinel-2 and PRISMA imagery are reported in the following.

Sentinel-2: The classification algorithm was firstly run considering the VNIR and SWIR bands (namely all the spectral bands except for Band 1, Band 9, and Band 10). Secondly, the Normalised Difference Vegetation Index (NDVI) was computed since it might provide benefits for distinguishing natural and artificial surfaces. Lastly, the building height layer was added as a further band. Four different band combinations were therefore tested, namely: (1) Sentinel-2 bands, (2) Sentinel-2 bands and NDVI layer, (3) Sentinel-2 bands and building height layer, (4) Sentinel-2 bands, NDVI layer, and building height layer.

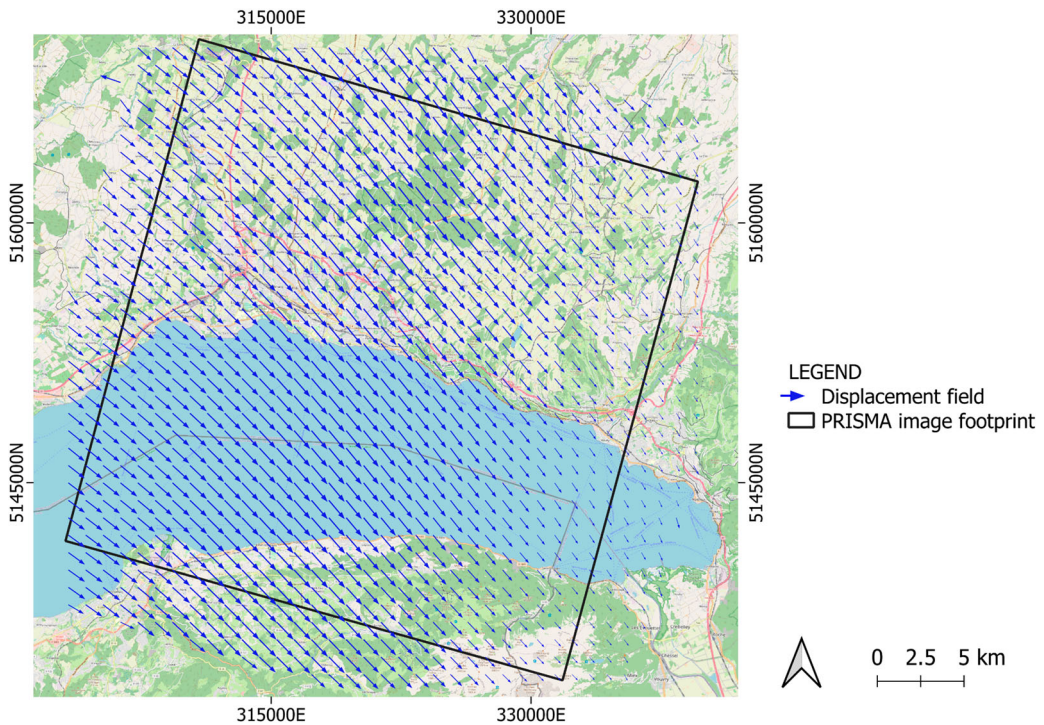


Figure 4. Example of displacement field, resampled to 1 km spatial resolution, estimated with GeFolki for the co-registration of PRISMA imagery (acquisition date: 6 September 2021). CRS: WGS84/UTM zone 32 N. Map data: OpenStreetMap contributors.

PRISMA: A first classification was performed considering only the PRISMA bands which are closest to the Sentinel-2 band central wavelengths (10 bands overall) to check whether similar spectral information provides consistent LCZ maps. The classification was then repeated considering all the PRISMA bands; this experiment was run with the aim of understanding whether an increased number of bands could be useful to achieve a higher quality LCZ map. Finally, the classification was carried out considering a linear combination of the original spectral bands, resulting in a way lower number of components. The linear combination of spectral bands was computed by applying a Principal Component Analysis (PCA) on the hyperspectral imagery, taking advantage of a dedicated tool provided within the Semi-Automatic Classification plugin (SCP) (Congedo 2021) in QGIS.

The reason behind the application of PCA on PRISMA imagery is twofold. On the one hand, PCA allows for an effective dimensionality reduction leading to faster classification performance and lower computational cost. On the other hand, only the relevant and uncorrelated information enclosed in the spectral information of the original bands is preserved using an adequate number of Principal Components (Gewers et al. 2022). Also, this prevents the negative impacts on the classification accuracy due to the limited training instances in proportion with the number of spectral features, which is known as Hughes effect (Taşkın, Kaya, and Bruzzone 2017). Several methods have been developed for the selection of a suitable number of PCs. However, a general indication is provided by the explained variance of the PCs (Song and Shin 2018). For all the images used in the present work, the first three to four PCs accounted for almost 100% of the cumulative explained variance, indicating that the first few PCs may be sufficient to explain data variation and thus retain the relevant information (see Figure 5). Some tests were carried out with the aim of measuring the sensitivity of the final classification accuracy to the number of selected PCs. For this reason, the RF algorithm was run on the first 3, 4, 5, and 10 PCs. The analysis was limited to a maximum of 10 PCs

which correspond to the number of retained Sentinel-2 bands. Furthermore, considering more than 10 PCs would not provide benefits in terms of explained variability of the data and would also require several other classifications to be run. An extensive sensitivity analysis focusing on the number of PCs and considering several case studies might be performed as future research to assess the possible generalisation of the obtained results.

To sum up, the following band combinations of PRISMA imagery were tested: (1) PRISMA bands closes to the Sentinel-2 band central wavelengths, (2) PRISMA bands, (3) PRISMA bands and building height layer, (4) first 3, 4, 5, and 10 PCs, separately, (5) first 3, 4, 5, and 10 PCs together with the building height layer, separately.

3.5. Image classification and accuracy assessment

A supervised pixel-based classification was applied to each satellite image and band combination. The Random Forest (RF) algorithm was adopted for this purpose (Breiman 2001). The RF was chosen as it provides high accuracy and fast computational time as well as an internal estimation of the classification unbiased error. Furthermore, RF has proven to yield satisfying classification performance when applied on hyperspectral imagery (Rissati, Molina, and Anjos 2020), which makes it suitable for comparing the classification maps obtained from Sentinel-2 and PRISMA data. In this study, the RF was applied through an R script using the *randomforest* library (Horning 2010). The same training samples were exploited for the classification of each satellite image and band combination.

A two-step post classification was applied to each LCZ map. As a first step, the classification sieve algorithm (with 5 pixels threshold) was used to smooth the noisy output of the RF algorithm. The GDAL (Geospatial Data Abstraction Library) implementation of the sieving filter available in QGIS was used for this purpose. Secondly, the maps obtained from the same band combination (and satellite sensor) referred to the four acquisition dates were merged through majority voting in QGIS, resulting in a single comprehensive LCZ map for each satellite image and band combination.

Classification performance was assessed in terms of classification accuracy using an independent 'out-of-bag' testing sample. Map accuracy was evaluated through common statistical measures computed from the confusion matrix, including Overall Accuracy (OA), Producer's Accuracy (PA), and User's Accuracy (UA). The confusion matrix and corresponding accuracy measures were computed in QGIS using the dedicated tool available within the SCP. Specifically, the accuracy was assessed for the post-processed seasonal classifications as well as for the synthetic maps obtained through majority voting. The statistics values of each LCZ class and map were compared through graphs and used to point out the best band combinations for LCZ mapping purposes and compare the classification performance of Sentinel-2 and PRISMA data.

4. Results and discussion

4.1. Classification accuracy of Sentinel-2 derived LCZ maps

A total number of 20 LCZ maps (including the final 4 maps obtained through majority voting) were computed using Sentinel-2 images. The accuracy of these maps is summarised in Figure 6, where the values of OA and class specific PA and UA are reported. Figure 7 represents the final LCZ map obtained by merging the Sentinel-2 bands together with the building height layer, corresponding to the highest OA value (equal to 97%). The other LCZ maps, together with the corresponding pixel-based confusion matrices, are reported in the Supplementary Material.

The OA resulted higher than 90% for all the classification outputs, with the highest values reported for the final classification map achieved with the application of majority voting (OA ranging from 95% to 97%). Similar values are also recorded for the PA and UA of the natural classes (namely, Scattered trees, Low plants, and Water) which are thus smoothly distinguished from the

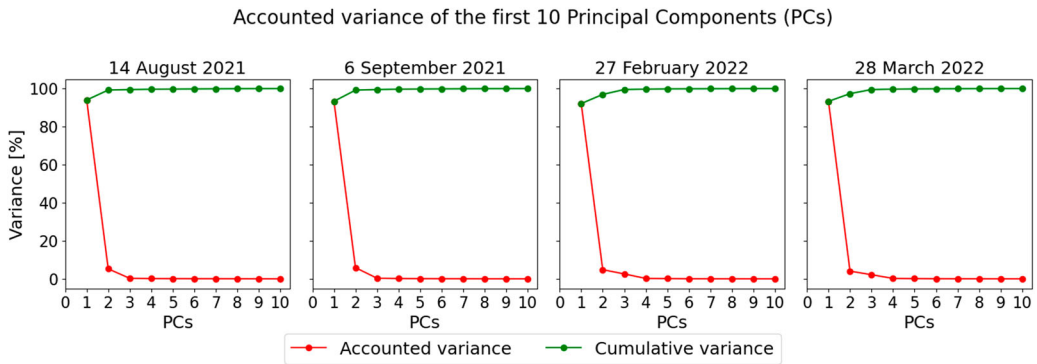


Figure 5. Accounted and cumulative variance of the first 10 Principal Components (PCs) of each PRISMA image.

artificial surfaces by the classification algorithm. This result applies considering all the acquisition dates as well as the different band combinations, meaning that the information provided by the original Sentinel-2 bands may be sufficient for the detection of natural classes.

Considering the built-up types, additional considerations may be pointed out. PA, and OA values for the built-up LCZ classes are generally lower than natural classes. For instance, using the Sentinel-2 bands, PA values are between 71% and 80% while UA ranges between 86% and 91%, on average. The worse performance of the classification algorithm in the detection of built-up types may be mainly due to their poor spectral separability at the Sentinel-2 band wavelengths. The NDVI layer yields a slight increase in the PA of the artificial surfaces including vegetated areas, i.e. open mid-rise and open low-rise classes (+9% and +5% respectively in the final map). However, this result is not supported by all date specific LCZ maps, therefore a robust conclusion cannot be drawn. For this reason, the NDVI was not used in the classification of PRISMA imagery. Contrarily, the building height layer provides benefits in terms of classification accuracy of built-up LCZ classes, despite some discrepancies in the accuracy can be found depending on the acquisition date. Nonetheless, average improvements of PA are between 5% and 10%, with the most significant improvement recorded in the final map (+20% for Compact mid-rise, +9% for Open mid-rise, and +12% for Open low-rise). The same conclusion does not hold for the Large low-rise class, which does not exhibit significant accuracy variations when the building height layer is integrated to the Sentinel-2 bands. Similar outputs were obtained by merging the NDVI layer and the building height layer to the Sentinel-2 spectral bands, suggesting that the building height data is indeed pivotal to properly detecting the different built-up types.

The difference of each predicted map with the best performing map, obtained using Sentinel-2 bands and building height layer, was computed, and the statistics of such differences are reported in the Supplementary Materials. The total difference, expressed in percentage of pixels, always resulted lower than 1% with differences being sparsely spatially distributed, indicating that the NDVI and building height layers produced a very limited change in the overall classification maps.

4.2. Classification accuracy of PRISMA derived LCZ maps

A total number of 55 LCZ maps (including 11 final maps obtained through majority voting) were computed with the PRISMA images. The values of classification accuracy for each map are reported in Figure 8. The best classification output is represented in Figure 9, corresponding to the final classification obtained using the first 10 PCs of the PRISMA bands. The other LCZ maps, together with the corresponding pixel-based confusion matrices, are reported in the Supplementary Material.

The high values of OA (higher than 90%) point out the good performance of the classification algorithm. A general consideration regards the natural classes: as for the previous experiments

Comparison of classification accuracy using different Sentinel-2 band combinations

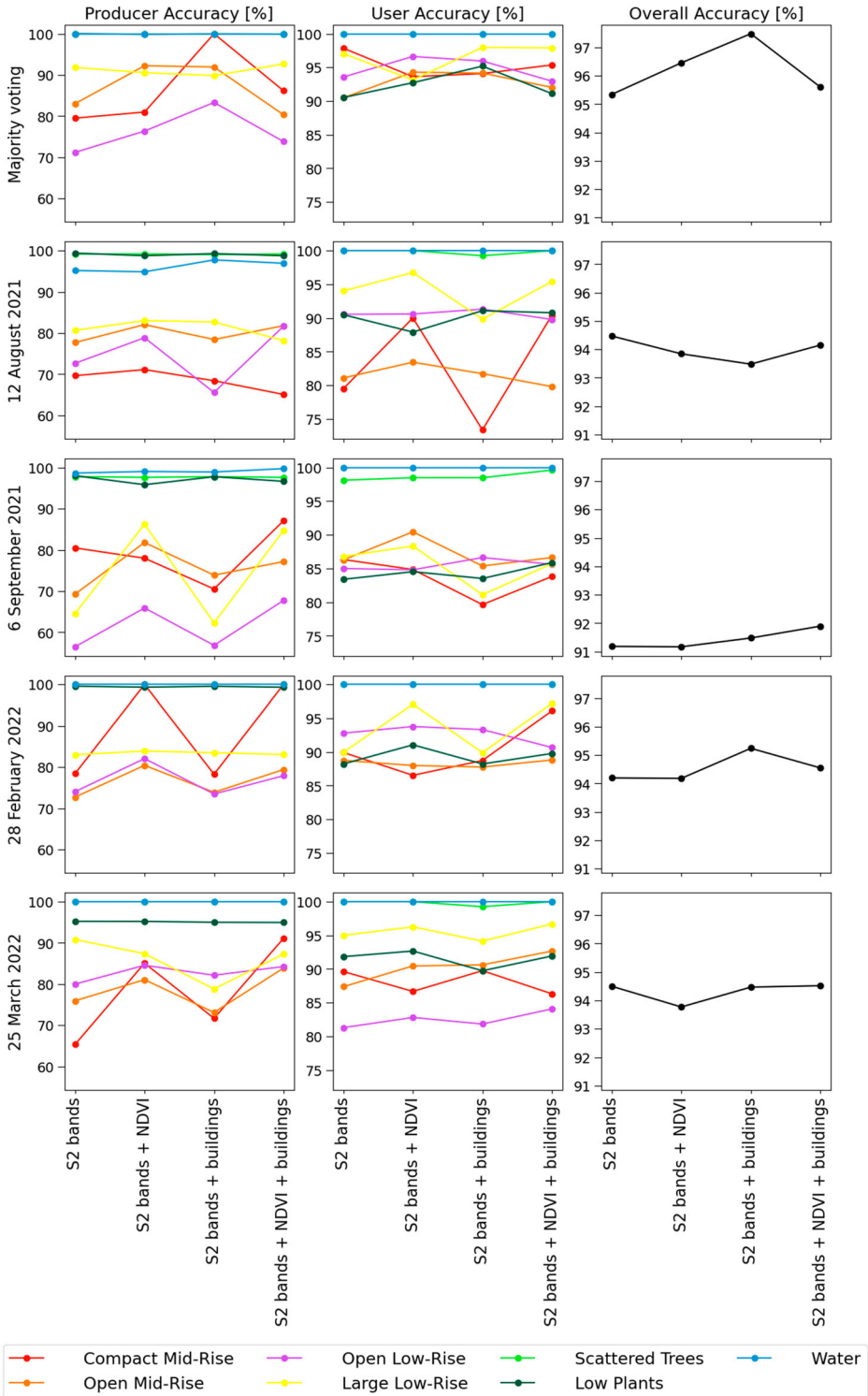


Figure 6. Comparison of classification accuracy using different band combinations (reported on the x axis) of Sentinel-2 imagery (acquisition dates reported on the y axis) and building height dataset.

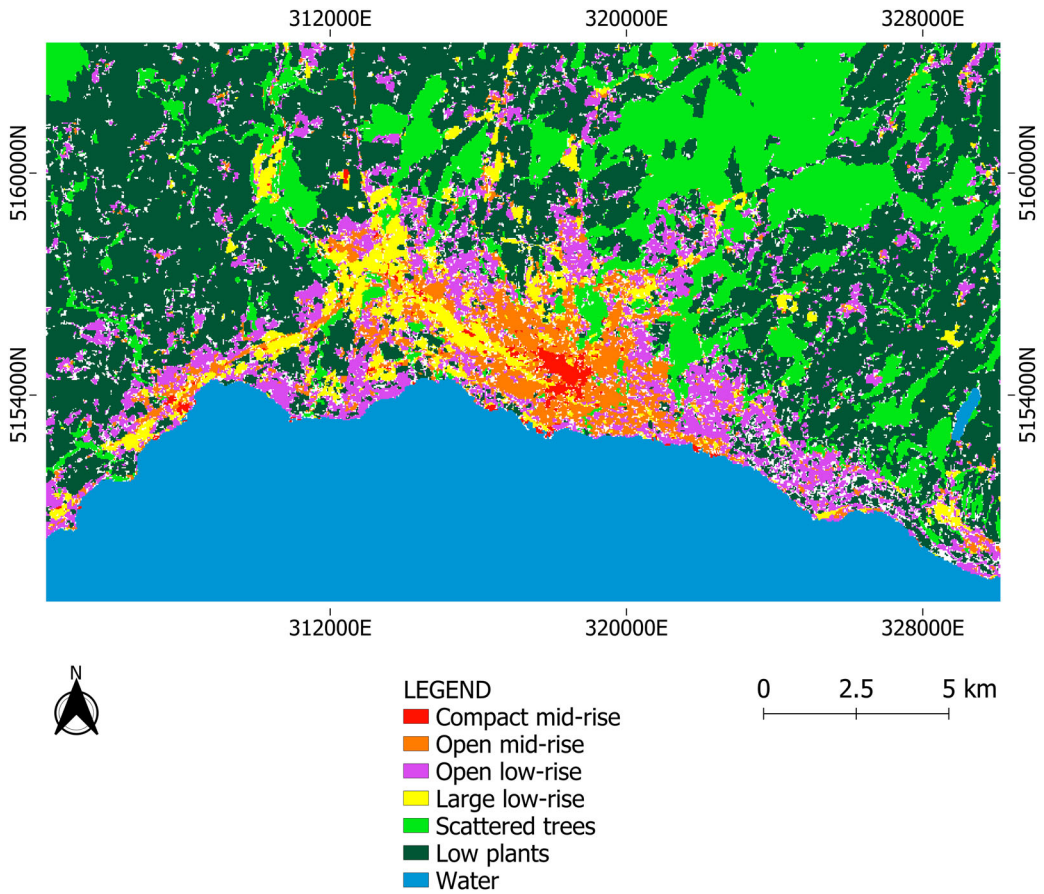


Figure 7. Final LCZ map obtained using Sentinel-2 imagery (majority voting applied to the four Sentinel-2 images). Band combination: Sentinel-2 bands plus building height layer. CRS: WGS84/UTM zone 32N.

involving Sentinel-2 imagery, a very good performance in the classification of Scattered trees, Low plants, and Water is recorded. Only the PRISMA spectral bands closest to the Sentinel-2 band central wavelengths were leveraged in the first experiment. Results clearly show that a different output is obtained compared to the classification maps derived from Sentinel-2 imagery. Despite some differences for the different acquisition dates, classification accuracy of built-up types turns out to be lower when using the corresponding PRISMA bands. This is especially true for the Open low-rise class (-21% for PA and -6% for UA in the final classification), whereas similar values are recorded for the natural areas. This result might be mainly due to the different spectral resolution of the two sensors – with the PRISMA spectral bands being narrower than the Sentinel-2 bands – which in fact makes the two multiband rasters quite different despite the relatively similar central wavelengths.

In view of the above considerations, the other experiments were carried out taking advantage of the whole spectral information provided by PRISMA. A significant improvement in classification performance – compared to the classification output of the previous test – is achieved when considering all the PRISMA bands. The increase in classification accuracy is evident for the built-up classes, with PA increase ranging from $+3\%$ (Open mid-rise) to $+10\%$ (Compact mid-rise), and UA increasing from $+2\%$ (Open low-rise) to $+10\%$ (Compact mid-rise) in the final LCZ maps. Despite the slightly different values, this consideration is supported by the different date specific classifications. A further improvement is obtained by including the building height layer as an

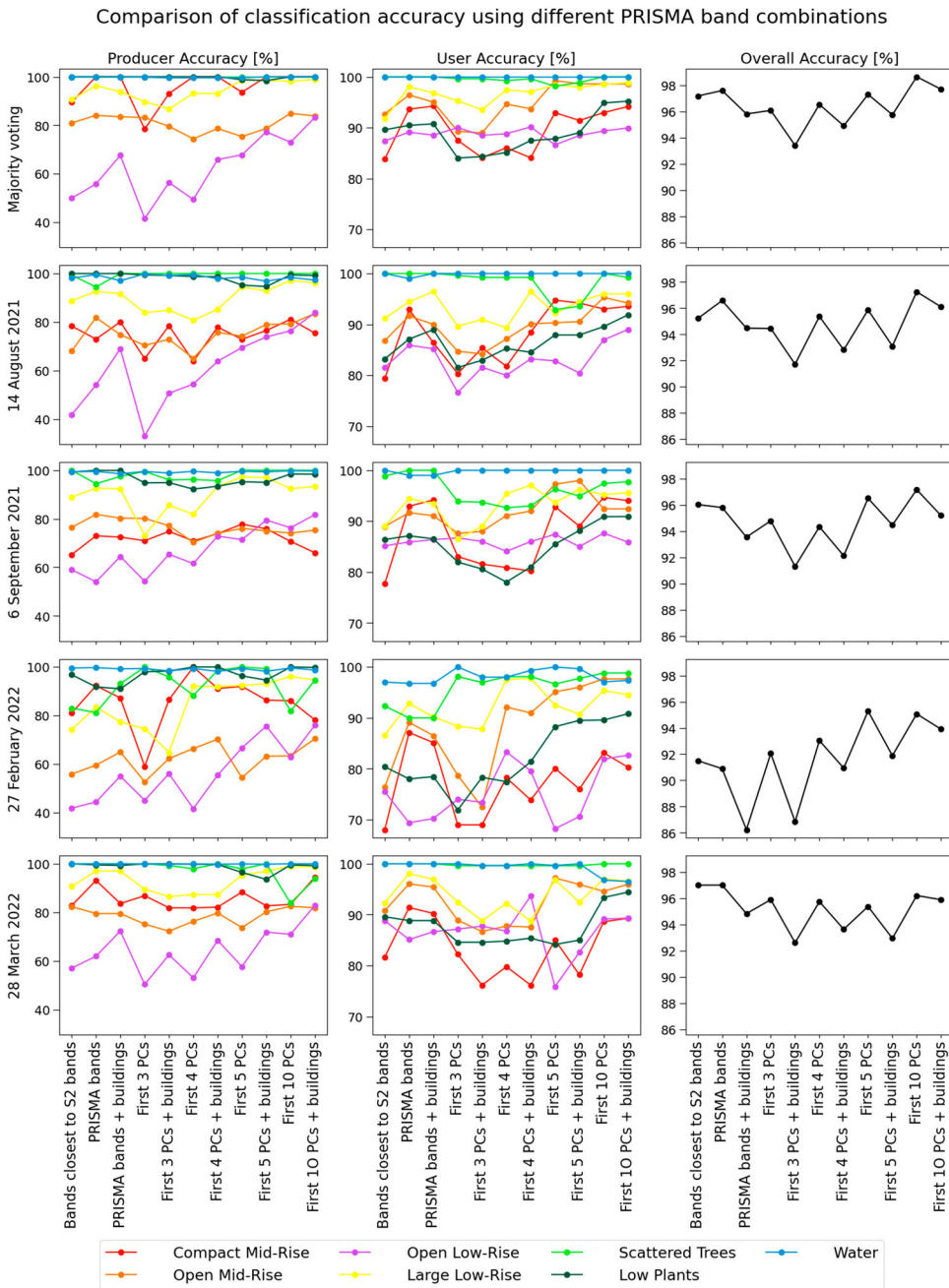


Figure 8. Comparison of classification accuracy using different band combinations (reported on the x axis) of PRISMA imagery (acquisition dates reported on the y axis) and building height dataset.

additional band, especially for the Open low-rise class (+12% in PA than using only the PRISMA bands). This result points out the benefits provided by the hyperspectral information for the classification of built-up LCZ types while confirming the building height data being a crucial information for LCZ mapping purposes.

A final experiment was performed which consisted in the use of different numbers of PCs. This allowed discarding the correlated information embedded in the PRISMA spectral bands while

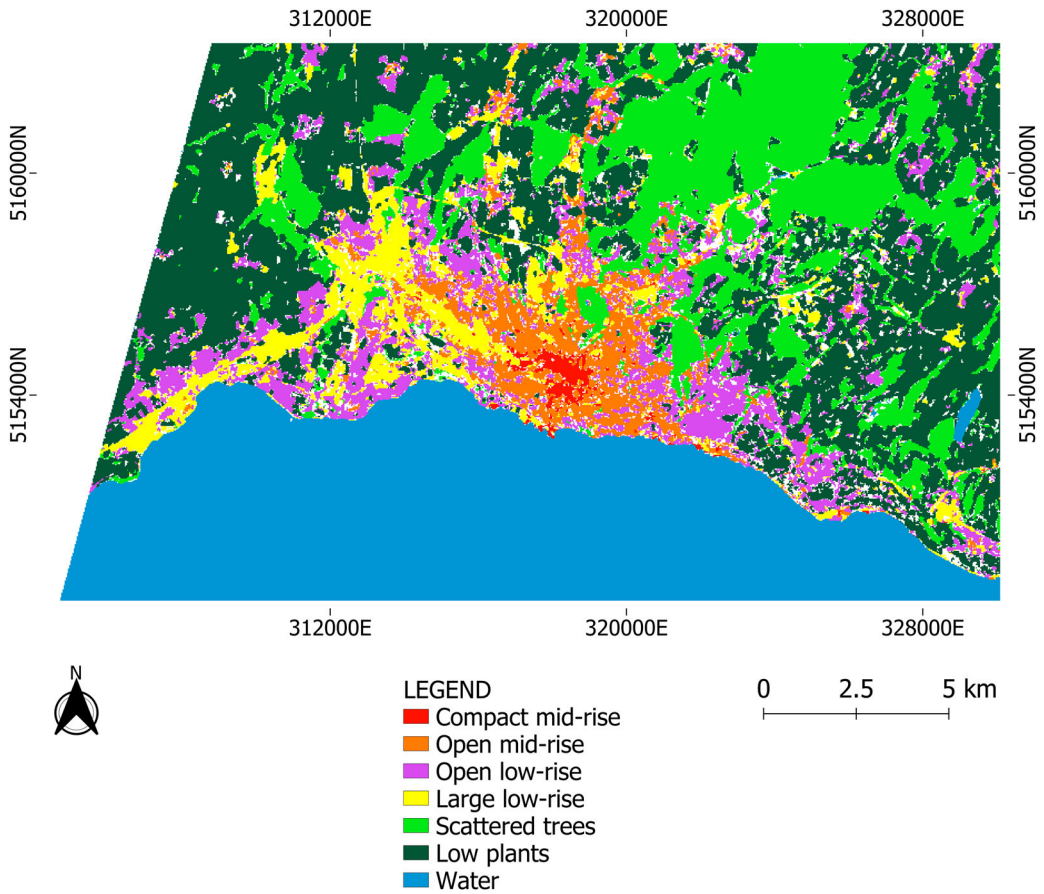


Figure 9. Final LCZ map obtained using PRISMA imagery (majority voting applied to the four PRISMA images). Band combination: First 10 Principal Components. CRS: WGS84/UTM zone 32N.

demanding way lower computational time. The results reported in Figure 8 show that classification accuracy increases with the number of PCs, with the best performance obtained considering the first 10 PCs. In this case, a general improvement in both PA and OA for the built-up LCZ types is achieved for all available images, except for the classifications of 22 February showing a different pattern in terms of accuracy as further discussed in Section 4.3. The PA of the Open low-rise class – which corresponds to the lowest PA considering the original PRISMA bands – increases up to 83% in the final map (+17% than considering the PRISMA bands and +23% compared to the first experiment). The use of the building height layer merged to the original PRISMA bands yields a further slight increase in the class specific PA and UA. Indeed, despite the similar value of OA (around 98%), the PA and OA of all LCZ classes turns out to be higher than 83% in the final classification.

The difference of each predicted map with the best performing map, obtained using the first 10 PCs, was also computed. The statistics of such differences, expressed as percentage of pixels, are reported in the Supplementary Material. The total pixel difference always resulted lower than 7%, and the differences showed a similar class specific pattern as well as a similar spatial distribution, with decreasing differences as the number of PCs increases. The difference between the best performing map and the one obtained using the original PRISMA bands was also mapped. Most of the differences are between Scattered trees and Low plants, Open low-rise and Low plants, and within the built-up types. Differences are more clustered across areas with a mixture of trees

and grasslands (Scattered trees/Low plants), and along the railway line station (Open mid-rise/Large low-rise), and generally along the borders of classes.

The quality of the final LCZ classification reported in Figure 9 was assessed using a reference product generated with the LCZ Generator (Demuzere, Kittner, and Bechtel 2021). The same training sample used for producing the LCZ maps was provided as an input to the software. The comparison between the two products is shown in Figure 10. Beside an Overall Accuracy 70%, the result indicates a higher confusion within the built-up classes. The confusion is mostly visible between Compact mid-rise and Open mid-rise, and Open low-rise and Low plants. This may be attributed to similar features shared by the mentioned classes, namely the presence of mid-rise buildings (Compact mid-rise and Open mid-rise) and vegetated areas (Open low-rise and Low plants). These results are in line with the confusion matrices obtained using the testing sample and shown in the Supplementary Material. However, using the map obtained with the LCZ Generator for the result assessment does not strictly amount to an accuracy evaluation, since this map cannot be considered more accurate than the map under evaluation. Therefore, the proposed approach must be intended as an inter-comparison, thereby allowing one to extract a consistency measure rather than actual accuracy metrics.

4.3. Comparison of Sentinel-2 and PRISMA derived LCZ maps

A comparison of classification accuracy using Sentinel-2 and PRISMA images is presented in Table 3. For the sake of conciseness, only the comparison of the final LCZ maps obtained through majority voting is reported. The whole comparison is provided in the Supplementary Material.

As stated in the previous section, different values of classification accuracy are obtained using the original Sentinel-2 bands and the closest 10 PRISMA bands. The latter band combination provides worse classification accuracy, especially for Open low-rise (−21% in PA). This result applies to the other LCZ maps and has to be considered for further analysis. Contrarily, using the whole set of PRISMA spectral bands yields best results for Compact mid-rise (+20% in PA), which is also confirmed by the other date specific classification maps, whereas a worse performance is recorded for Open low-rise (−15% in PA). Overall, a slight improvement in the classification performance is achieved using the PRISMA bands. Nonetheless, this result does not convincingly prove that a general benefit is provided by the hyperspectral data, considering the slight accuracy increase compared to the way longer computational time. The improvement in classification accuracy is mostly attributable to the richer spectral information carried by the PRISMA bands. This is clearly visible in Figure 11 that depicts the median spectral signature of the training samples per LCZ class for both PRISMA and Sentinel-2 images.

The high spectral resolution of the PRISMA sensor positively influences the classification results. Except for the class water, which shows its typical spectral signature (i.e. water exhibits reflection

Table 3. Increase/decrease (Δ) in Producer's Accuracy (PA) and User's Accuracy (UA) using different PRISMA band combinations compared to the classification obtained with Sentinel-2 bands (final classifications computed through majority voting).

Class name	PRISMA band combination							
	Classification with Sentinel-2 bands		PRISMA bands closest to Sentinel-2 bands		PRISMA bands		First 10 PRISMA Principal Components	
	PA [%]	UA [%]	Δ PA [%]	Δ UA [%]	Δ PA [%]	Δ UA [%]	Δ PA [%]	Δ UA [%]
Compact mid-rise	79.5	97.8	+10.0	−14.0	+20.5	−4.2	+20.5	−4.9
Open mid-rise	83.0	90.5	−2.0	+2.2	+1.1	+5.9	+1.9	+8.1
Open low-rise	71.2	93.6	−21.2	−6.1	−15.4	−4.5	+1.8	−4.2
Large low-rise	91.8	97.0	−1.2	−5.3	+4.5	+1.0	+6.3	+1.4
Scattered trees	100	100	0	0	0	0	0	0
Low plants	100	90.5	0	−0.9	0	−0.1	0	+4.3
Water	100	100	−0.1	0	0	0	0	0

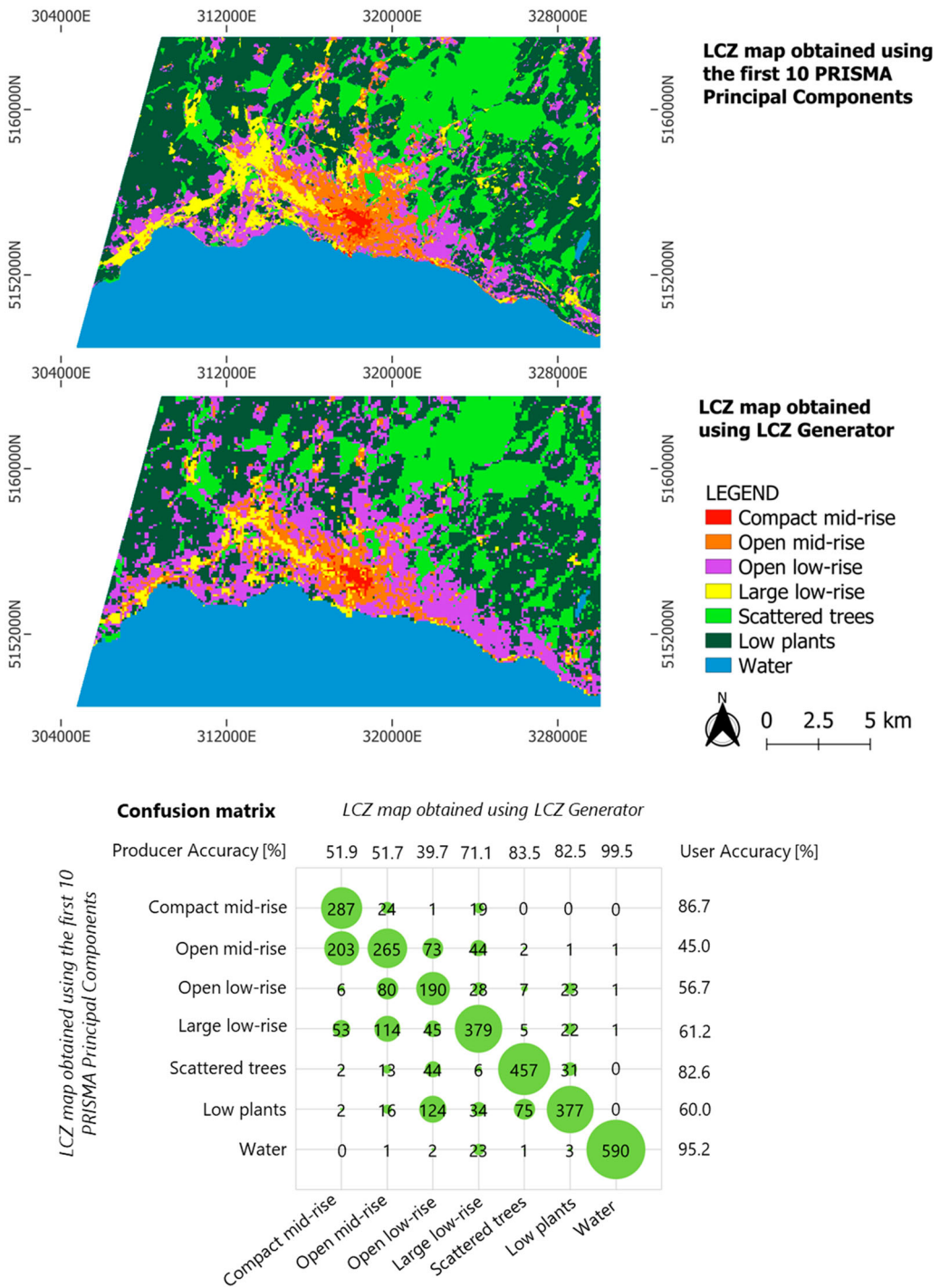


Figure 10. Comparison between the final LCZ map obtained using the first 10 PRISMA Principal Components (after majority voting) (above panel) and the LCZ map obtained using the LCZ Generator (middle panel), and corresponding confusion matrix (low panel).

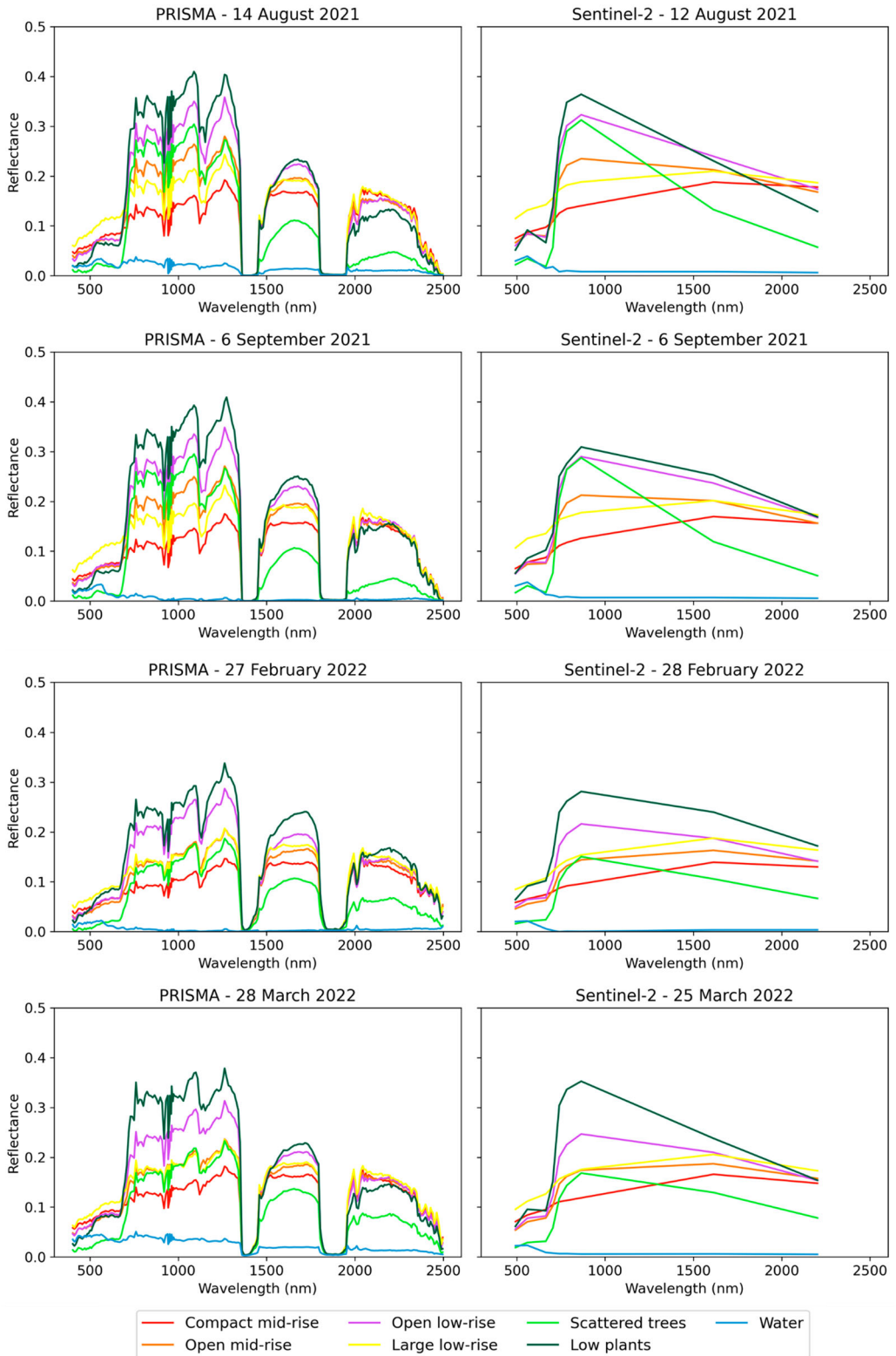


Figure 11. Median spectral signatures of the training samples per LCZ class for each date-specific PRISMA and Sentinel-2 acquisition.

primarily within the visible light spectrum while most of the near infrared signal is absorbed), the other classes have a similar spectral behaviour. The main differences are evident for infrared wavelengths and in the red edge. Major spectral differences among the classes are found for the summer period (August and September), with respect to the winter (February and March), which justifies the lower accuracy values of the winter LCZ maps. Specifically, the reduced performance of PRISMA for the February dataset may be attributed to the reduced spectral separability of the classes, resulting in a reduced classification performance.

A more robust improvement is recorded using the first 10 PCs of the PRISMA bands, corresponding to an increase in the accuracy of all built-up classes independently of the image acquisition date. This band combination outperforms the original Sentinel-2 data. This is especially true for Compact mid-rise (+20% in PA) and Large low-rise (+6.3% in PA), resulting in OA equal to 99%. This preliminary outcome suggests the first 10 PCs being a good compromise for achieving a fast computational performance as well as a satisfying classification accuracy and will be further investigated.

5. Conclusions and future developments

In this paper, a comparison of classification performance of multispectral (Sentinel-2) and hyperspectral (PRISMA) imagery for LCZ mapping was presented, considering the city of Lausanne (Switzerland) as a case study. Four seasonal acquisitions of the PRISMA mission and four corresponding Sentinel-2 images were selected to consider the seasonal variations of vegetation within the LCZ maps as well as increase classification accuracy. Training and testing samples were independently collected by leveraging ancillary geodata including the building height layer of the study area. Several tests were carried out considering different band combinations of the two image types with the aim of investigating the contribute of the spectral bands to the classification accuracy of each LCZ type.

Results pointed out a satisfying performance of the classification algorithm applied on both multispectral and hyperspectral imagery. Despite some differences in the classification maps for the different acquisition dates, some general conclusions may be pointed out. Firstly, the building height dataset turned out to be pivotal to increase the accuracy values of the built-up LCZ classes – as already disclosed by previous research works – while no significant benefits were provided by the NDVI layer. Secondly, increasing the number of PRISMA spectral bands yields an improvement in the classification accuracy owing to the increased spectral separability of the LCZ classes. Nonetheless, the whole collection of PRISMA spectral bands did not provide a significant increase in the classification accuracy compared to the original Sentinel-2 bands. The reason might be twofold. On the one hand, the quality of the PRISMA imagery may be relatively lower compared to the Sentinel-2 data. The second reason may be connected to the different spectral resolution of the two satellite sensors which might partially affect the result. The use of the first 10 PCs of the PRISMA spectral bands provided a further improvement in the classification accuracy while requiring a way lower computational cost. Indeed, the classification performed using the first 10 PCs provides an improvement in terms of accuracy compared to the result obtained by exploiting the original Sentinel-2 bands. It should be noted that the result obtained in terms of optimal number of PCs is specific to the selected case study and cannot be generalised to other regions. Further experiments should be run to validate this conclusion. Nevertheless, the outcome suggests the PCA as a powerful tool for decoupling the relevant information out of the noisy and correlated data embedded within the PRISMA hyperspectral data. The study also points out that using hyperspectral imagery does not necessarily yield to an improved LCZ classification accuracy unless a suitable feature selection is performed.

Future analyses will focus on the improvement of PRISMA imagery pre-processing, including image co-registration (e.g. exploiting the 5 m resolution panchromatic band) and preliminary band selection (e.g. removing the atmospheric water absorption bands and low signal-to-noise

ratio bands). Furthermore, the collection of a higher number of Sentinel-2 and PRISMA imagery (mainly depending on the PRISMA data availability) may allow for a more insightful investigation of the seasonal effects which could not be properly pointed out in the present work. These activities could be helpful for increasing the accuracy of the final LCZ map. Lastly, future developments will also concentrate on the increase of PRISMA imagery spatial resolution – which is originally equal to 30 m – through the application of pan-sharpening and super-resolution techniques. The coupling of high spatial and spectral resolution may provide further benefits to the LCZ classification.

Acknowledgements

This work was carried out in the frame of a PhD Program in Environmental and Infrastructure Engineering, funded by the Italian PON (Programma Operativo Nazionale) project scholarship entitled ‘Geospatial Enablement for Climate Change Impact Mitigation on Cities and Urban Resilience Acceleration’. This paper is based on the dataset made available by the Italian Space Agency (ASI): Data/Information generated by the authors under a license from ASI Original PRISMA Product – © ASI – 2021/2022. The authors would like to thank Mr. Olivier Travaglini, Cadaster and GeoInformation Department of the Vaud State, for providing the ancillary data (e.g. building height) of the city of Lausanne.

Disclosure statement

No potential conflict of interest was reported by the author(s).

ORCID

Alberto Vavassori  <http://orcid.org/0000-0001-5329-2789>

Gregory Giuliani  <http://orcid.org/0000-0002-1825-8865>

Maria Antonia Brovelli  <http://orcid.org/0000-0003-3161-5561>

References

- Aslam, A., and I. A. Rana. 2022. “The use of Local Climate Zones in the Urban Environment: A Systematic Review of Data Sources, Methods, and Themes.” *Urban Climate* 42: 101120. <https://doi.org/10.1016/j.uclim.2022.101120>.
- Bechtel, B., P. J. Alexander, C. Beck, J. Böhner, O. Brousse, J. Ching, M. Demuzere, et al. 2019a. “Generating WUDAPT Level 0 Data – Current Status of Production and Evaluation.” *Urban Climate* 27: 24–45. <https://doi.org/10.1016/j.uclim.2018.10.001>.
- Bechtel, B., P. J. Alexander, C. Beck, J. Böhner, O. Brousse, J. Ching, M. Demuzere, et al. 2019b. “Generating WUDAPT Level 0 Data – Current Status of Production and Evaluation.” *Urban Climate* 27: 24–45. <https://doi.org/10.1016/j.uclim.2018.10.001>.
- Bechtel, B., P. J. Alexander, J. Böhner, J. Ching, O. Conrad, J. Feddema, G. Mills, L. See, and I. Stewart. 2015. “Mapping Local Climate Zones for a Worldwide Database of the Form and Function of Cities.” *ISPRS International Journal of Geo-Information* 4: 199–219. <https://doi.org/10.3390/ijgi4010199>.
- Bocher, E., J. Bernard, E. Wiederhold, F. Leconte, G. Petit, S. Palominos, and C. Noûs. 2021. “GeoClimate: A Geospatial Processing Toolbox for Environmental and Climate Studies.” *Journal of Open Source Software* 6: 3541. <https://doi.org/10.21105/joss.03541>.
- Breiman, L. 2001. “Random Forests.” *Machine Learning* 45: 5–32. <https://doi.org/10.1023/A:1010933404324>.
- Brigot, G., E. Colin-Koeniguer, A. Plyer, and F. Janez. 2016. “Adaptation and Evaluation of an Optical Flow Method Applied to Coregistration of Forest Remote Sensing Images.” *IEEE Journal of Selected Topics in Applied Earth Observations and Remote Sensing* 9: 2923–2939. <https://doi.org/10.1109/JSTARS.2016.2578362>.
- Chapman, S., M. Thatcher, A. Salazar, J. E. M. Watson, and C. A. McAlpine. 2019. “The Impact of Climate Change and Urban Growth on Urban Climate and Heat Stress in a Subtropical City.” *International Journal of Climatology* 39: 3013–3030. <https://doi.org/10.1002/joc.5998>.
- Ching, J., G. Mills, B. Bechtel, L. See, J. Feddema, X. Wang, C. Ren, et al. 2018. “WUDAPT: An Urban Weather, Climate, and Environmental Modeling Infrastructure for the Anthropocene.” *Bulletin of the American Meteorological Society* 99: 1907–1924. <https://doi.org/10.1175/BAMS-D-16-0236.1>.
- Congedo, L. 2021. “Semi-Automatic Classification Plugin: A Python Tool for the Download and Processing of Remote Sensing Images in QGIS.” *Journal of Open Source Software* 6: 3172. <https://doi.org/10.21105/joss.03172>.
- Copernicus Urban Atlas. 2018. <https://land.copernicus.eu/local/urban-atlas/urban-atlas-2018>.

- Demuzere, M., J. Kittner, and B. Bechtel. 2021. "LCZ Generator: A Web Application to Create Local Climate Zone Maps." *Frontiers in Environmental Science* 9: 637455. <https://doi.org/10.3389/fenvs.2021.637455>.
- Fung, K. Y., Z.-L. Yang, and D. Niyogi. 2022a. "Improving the Local Climate Zone Classification with Building Height, Imperviousness, and Machine Learning for Urban Models." *Computational Urban Science* 2: 16. <https://doi.org/10.1007/s43762-022-00046-x>.
- Fung, K. Y., Z.-L. Yang, and D. Niyogi. 2022b. "Improving the Local Climate Zone Classification with Building Height, Imperviousness, and Machine Learning for Urban Models." *Computational Urban Science* 2: 1336. <https://doi.org/10.1007/s43762-022-00046-x>.
- Gewers, F.L., Ferreira, G.R., Arruda, H.F. De, Silva, F.N., Comin, C.H., Amancio, D.R., Costa, L. Da F. 2022. "". *ACM Computing Surveys* 54: 1-34. <https://doi.org/10.1145/3447755>.
- Horning, N. 2010. "Random Forests: An Algorithm for Image Classification and Generation of Continuous Fields Data Sets". In *Paper Presented at the International Conference on Geoinformatics for Spatial Infrastructure Development in Earth and Allied Sciences*, Osaka, Japan, December 9–11.
- Kim, S. W., and R. D. Brown. 2021. "Urban Heat Island (UHI) Intensity and Magnitude Estimations: A Systematic Literature Review." *Science of the Total Environment* 779: 146389. <https://doi.org/10.1016/j.scitotenv.2021.146389>.
- Köppen, W. 1984. "Die Wärmzonen der Erde, Nach der Dauer der Heissen, Gemässigten und Kalten Zeit und Nach der Wirkung der Wärme auf die Organische Welt Betrachtet." *Meteorologische Zeitschrift* 1: 5–226.
- Kotharkar, R., A. Ghosh, S. Kapoor, and D. G. K. Reddy. 2022. "Approach to Local Climate Zone Based Energy Consumption Assessment in an Indian City." *Energy and Buildings* 259: 111835. <https://doi.org/10.1016/j.enbuild.2022.111835>.
- Liang, Y., W. Song, S. Cao, and M. Du. 2023. "Local Climate Zone Classification Using Daytime Zhuhai-1 Hyperspectral Imagery and Nighttime Light Data." *Remote Sensing* 15: 3351. <https://doi.org/10.3390/rs15133351>.
- Lu, B., Y. He, and P. D. Dao. 2019. "Comparing the Performance of Multispectral and Hyperspectral Images for Estimating Vegetation Properties." *IEEE Journal of Selected Topics in Applied Earth Observations and Remote Sensing* 12: 1784–1797. <https://doi.org/10.1109/JSTARS.2019.2910558>.
- Mouzourides, P., A. Eleftheriou, A. Kyprianou, J. Ching, and M. K.-A. Neophytou. 2019. "Linking Local-Climate-Zones Mapping to Multi-Resolution-Analysis to Deduce Associative Relations at Intra-Urban Scales Through an Example of Metropolitan London." *Urban Climate* 30. <https://doi.org/10.1016/j.uclim.2019.100505>.
- Mushore, T. D., T. Dube, M. Manjowe, W. Gumindoga, A. Chemura, I. Rousta, J. Odindi, and O. Mutanga. 2019. "Remotely Sensed Retrieval of Local Climate Zones and Their Linkages to Land Surface Temperature in Harare Metropolitan City, Zimbabwe." *Urban Climate* 27: 259–271. <https://doi.org/10.1016/j.uclim.2018.12.006>.
- Oliveira, A., A. Lopes, and S. Niza. 2020. "Local Climate Zones in Five Southern European Cities: An Improved GIS-Based Classification Method Based on Copernicus Data." *Urban Climate* 33: 100631. <https://doi.org/10.1016/j.uclim.2020.100631>.
- PRISMA Products Specification Document. 2020. http://prisma.asi.it/missionsselect/docs/PRISMA%20Product%20Specifications_Is2_3.pdf.
- Rissati, J. V., P. C. Molina, and C. S. Anjos. 2020. "Hyperspectral Image Classification Using Random Forest and Deep Learning Algorithms". In *Paper Presented at the IEEE Latin American GRSS & ISPRS Remote Sensing Conference (LAGIRS)*, Santiago, Chile, March 22–27. <https://doi.org/10.1109/LAGIRS48042.2020.9165588>.
- Sigler, L., J. Gilbert, and G. Villalba. 2022. "Exploring Methods for Developing Local Climate Zones to Support Climate Research." *Climate* 10: 109. <https://doi.org/10.3390/cli10070109>.
- Song, J., and S. J. Shin. 2018. "Stability Approach to Selecting the Number of Principal Components." *Computational Statistics* 33: 1923–1938. <https://doi.org/10.1007/s00180-018-0826-7>.
- Stewart, I. D., and T. R. Oke. 2012. "Local Climate Zones for Urban Temperature Studies." *Bulletin of the American Meteorological Society* 93: 1879–1900. <https://doi.org/10.1175/BAMS-D-11-00019.1>.
- Stewart, I. D., T. R. Oke, and E. S. Krayenhoff. 2013. "Evaluation of the 'Local Climate Zone' Scheme Using Temperature Observations and Model Simulations." *International Journal of Climatology* 34: 1062–1080. <https://doi.org/10.1002/joc.3746>.
- Sukhanov, S., I. Tankoyev, J. Louradour, R. Heremans, D. Trofimova, and C. Debes. 2017. "Multilevel Ensembling for Local Climate Zones Classification". In *Paper Presented at the IEEE International Geoscience and Remote Sensing Symposium (IGARSS)*, Fort Worth, TX, USA, July 23–28.
- Taşkın, G., H. Kaya, and L. Bruzzone. 2017. "Feature Selection Based on High Dimensional Model Representation for Hyperspectral Images." *IEEE Transactions on Image Processing* 26: 2918–2928. <https://doi.org/10.1109/TIP.2017.2687128>.
- Verdonck, M.-L., M. Demuzere, H. Hooyberghs, C. Beck, J. Cyrus, A. Schneider, R. Dewulf, and F. Van Coillie. 2018. "The Potential of Local Climate Zones Maps as a Heat Stress Assessment Tool, Supported by Simulated air Temperature Data." *Landscape and Urban Planning* 178: 183–197. <https://doi.org/10.1016/j.landurbplan.2018.06.004>.